Volume 19, Number 1, 2026. pp. 1-12

Jordan Journal of Physics

ARTICLE

Fe-Sb Thin Films Obtained by Thermal Evaporation of Nanostructured Milled Powder: Investigation of Structural and Magnetic Properties

A. Hafs[a,b], **T. Hafs**[c] and **D. Berdjane**[d]

[a] *Department of Physics, University of Chadli Bendjedid, P.O. Box 73, El Tarf, 36000 Algeria.*

[b] *LEREC Laboratory, Department of Physics, University of Badji Mohktar, P.O. Box 12, Annaba, 23000 Algeria.*

[c] *LERICA Laboratory, Department of Electronics, University of Badji Mokhtar; P.O. Box 12, Annaba, 23000 Algeria.*

[d] *Research Center in Industrial Technologies (CRTI), P.O. Box 64, Cheraga, Algiers 16014, Algeria.*

DOI: **https://doi.org/10.47011/19.1.1**

Received on: 05/11/2024; *Accepted on: 07/09/2025*

Abstract: Nanostructured $Fe_{90}Sb_{10}$ (wt.%) alloys were synthesized by mechanically alloying pure iron and antimony powders in a high-energy planetary ball mill. The milling duration was optimized to achieve a nanostructured mixture and form a supersaturated solid solution of α-Fe(Sb). Subsequently, thin films were fabricated through thermal evaporation (physical vapor deposition) under a vacuum of 2.1×10^{-5} mbar, utilizing an electrically heated tungsten boat and the supersaturated solid solution α-Fe(Sb) powder obtained via mechanical alloying. The films were deposited on glass substrates. This study investigates the influence of milling time and film thickness on the structural and magnetic properties of $Fe_{90}Sb_{10}$ powders and thin films. Structural and magnetic characterizations were performed using X-ray diffraction (XRD), scanning electron microscopy (SEM), and vibrating sample magnetometry (VSM). The Fe(Sb) solid solution phase was identified after 12 hours of milling, with a particle size of approximately 18.16 nm with microstrain increasing to 0.19% after 36 hours. SEM analysis revealed a more homogeneous particle distribution as milling time increased. Furthermore, as the film thickness increased from 16 nm to 90 nm, a steady decrease was observed in the lattice parameter, accompanied by an increase in the average crystallite size from 5.9 nm to 16.8 nm and a slight increase in microstrain. In parallel, the coercive field dropped from 6.64 Oe to 3.05 Oe, suggesting improved magnetic softness in thicker films.

Keywords: Thin films, FeSb solid solution, Microstructure, X-ray diffraction (XRD), Vibrating sample magnetometry (VSM).

1. Introduction

In recent years, the field of nanomaterials and nanotechnologies has emerged as one of the most captivating and dynamic domains of scientific inquiry, attracting the attention of researchers and innovators across the globe [1-5]. Its appeal is rooted in the vast potential it holds, spanning both the fundamental principles of science and the practical applications that can transform industries and technologies [6, 7]. Among the diverse array of nanomaterials that have sparked tremendous interest and exploration, ferromagnetic thin films stand out as a category of paramount significance. From a technological perspective, these thin films have found their place at the intersection of scientific ingenuity and practical utility, offering a myriad of applications that extend far beyond the

Corresponding Author: Ali Hafs **Email**: hafs-ali@univ-eltarf.dz

conventional boundaries of materials science [8, 9].

At the heart of this burgeoning field is a profound appreciation for the potential that nanoscale materials and technologies provide. The ability to engineer, manipulate, and control matter at the atomic and molecular level has unlocked an astonishing realm of possibilities. It enables the creation of materials with finely-tuned properties and exceptional functionalities, serving as a bridge between theoretical knowledge and real-world applications. Within this transformative landscape, ferromagnetic thin films emerge as a remarkable subset, possessing the power to reshape how we interact with and harness magnetic properties [10].

From a technological standpoint, ferromagnetic thin films are not merely of academic interest but are invaluable tools with a diverse range of applications. They hold the potential to serve as the foundation for magnetic recording media, supporting data storage technologies that underpin our modern digital world. Whether it's the magnetic hard drives storing vast troves of information or the delicate magnetic heads that read and write data with astonishing precision, ferromagnetic thin films underpin these systems, exemplifying their indispensable role in our daily lives [11, 12].

However, the significance of ferromagnetic thin films extends well beyond the realm of data storage. Their influence reaches into other corners of the scientific and technological landscape, illuminating new pathways for innovation. These materials can be integrated into sensor technologies, enabling the development of highly sensitive detectors for various physical phenomena. They offer potential solutions for enhancing the efficiency of energy conversion and storage systems, which have become paramount in addressing global challenges such as climate change. Moreover, they hold promise in the development of spintronics, a burgeoning field that explores the utilization of electron spin as a fundamental unit of information, thus opening new vistas in computing and electronics [13].

In the grand tapestry of nanomaterials and nanotechnologies, ferromagnetic thin films not only represent a fascinating subject of study but also a testament to the transformative power of scientific discovery. The fusion of fundamental insights with practical applications serves as the cornerstone of progress in the 21st century. As this study investigates the world of ferromagnetic thin films, we find ourselves at the nexus of scientific curiosity and technological innovation [14, 15].

This study aims to investigate the influence of thickness on the structural and magnetic properties of thin layers of α-Fe(Sb) solid solution deposited via vacuum thermal evaporation on glass substrates. Previous studies have explored the structural and magnetic properties of Fe-based alloys and thin films, with a particular focus on Fe-Sb systems. These studies have revealed key insights into the evolution of these properties with milling time, as well as the impact of film thickness on lattice parameters, crystallite size, and coercivity. Notably, the formation of solid solution phases and changes in the magnetic behavior of Fe-Sb alloys have been reported, which serve as a foundation for understanding the results presented in this study.

2. Experimental

2.1. Materials and Methods

We employed mechanical alloying to produce FeSb alloy particles, forming a supersaturated solid solution of FeSb. Our starting materials included commercially available Fe (Alfa-Aesar, 99.9%, < 10 μm) and Sb (Alfa-Aesar, 99.8%, < 40 μm) powders. We utilized a planetary RETSCH PM 400 ball mill, operating at a rotational speed of 350 rpm and a ball-to-powder weight ratio of 15:1. The milling experiments were conducted within a controlled argon atmosphere [16] to prevent oxidation during the milling process. In addition, the mill operated for 1 hour followed by a 30-minute break. The selected effective milling durations were as follows: 2, 4, 8, 12, 16, and 36 hours.

The deposition of FeSb solid-solution films onto thoroughly cleaned Corning glass substrates was accomplished through the thermal evaporation method employing resistive heating. We utilized an MECA 2000 evaporator, loaded with FeSb supersaturated powder contained in a tungsten boat. The distance between the substrate and the source was optimized to 50 mm, and the process was conducted at a pressure of 2.1×10^{-5} mbar. Importantly, the film deposition was carried out at room temperature without any substrate heating.

2.2. Characterization

The X-ray diffraction (XRD) characterization of milled powders at different milling times and thin films at various thicknesses was carried out using a Bruker D8 Advance Eco X-ray diffractometer equipped with Cu Kα radiation from a copper anode at 40 kV and 40 mA, operating at a wavelength of λ = 1.541874 Å, in a (θ–2θ) Bragg-Brentano geometry. The XRD analysis was conducted at an ambient temperature of 25°C. Employing the Rietveld method, the diffractograms were refined using the MAUD software (version 2.22), a specialized application designed for materials analysis through diffraction techniques [16].

The Quantum 250 – FEI electron microscope (SEM) was employed to capture micrographs, to examine and characterize the morphology and uniformity of powder mixtures obtained at different grinding durations and thin films at various thicknesses. Subsequently, magnetic assessments were performed at room temperature using a MicroSense V7 model vibrating sample magnetometer (VSM). The magnetometer (VSM) was used to assess the magnetic properties of the powders and thin films, specifically focusing on hysteresis cycles. This assessment involves determining parameters such as magnetization saturation (Ms), coercivity (Hc), and remanent magnetization (Mr), based on the applied magnetic field, with a maximum of 18 kOe.

3. Results and Discussion

3.1. Fe–10Sb (wt.%) Milled Powders

In Fig. 1(a), a set of X-ray diffraction (XRD) patterns for Fe–10Sb (wt.%) powder mixtures is presented. These patterns were obtained after subjecting the mixtures to mechanical alloying (MA) for varying durations at room temperature. The XRD peaks were recorded for the pure iron and antimony components of the initial powder mixture (designated as 0 h in Fig. 1(a)). The recorded peaks revealed reflections corresponding to iron, which has a body-centered cubic (bcc) structure, specifically along the planes (110), (200), (211), (220), and (310). Meanwhile, antimony exhibited a rhombohedral structure, as evidenced by reflections along the planes (012), (104), (040), and (116). Following 12 hours of milling, a noteworthy observation was made: the disappearance of Sb peaks entirely, accompanied by a subtle shift of the Fe-related peaks towards smaller angles (see Fig. 1(b)). This observation confirms the dissolution of Sb atoms into the Fe lattice, resulting in the creation of bcc solid solutions denoted as Fe (Sb). The minor angular shift is ascribed to the development of the Fe (Sb) solid solution and the introduction of first-order internal stress induced during milling. This first-order angular stress operates at a macroscopic level, altering the lattice parameter and consequently causing an angular shift in the XRD peaks [17-19].

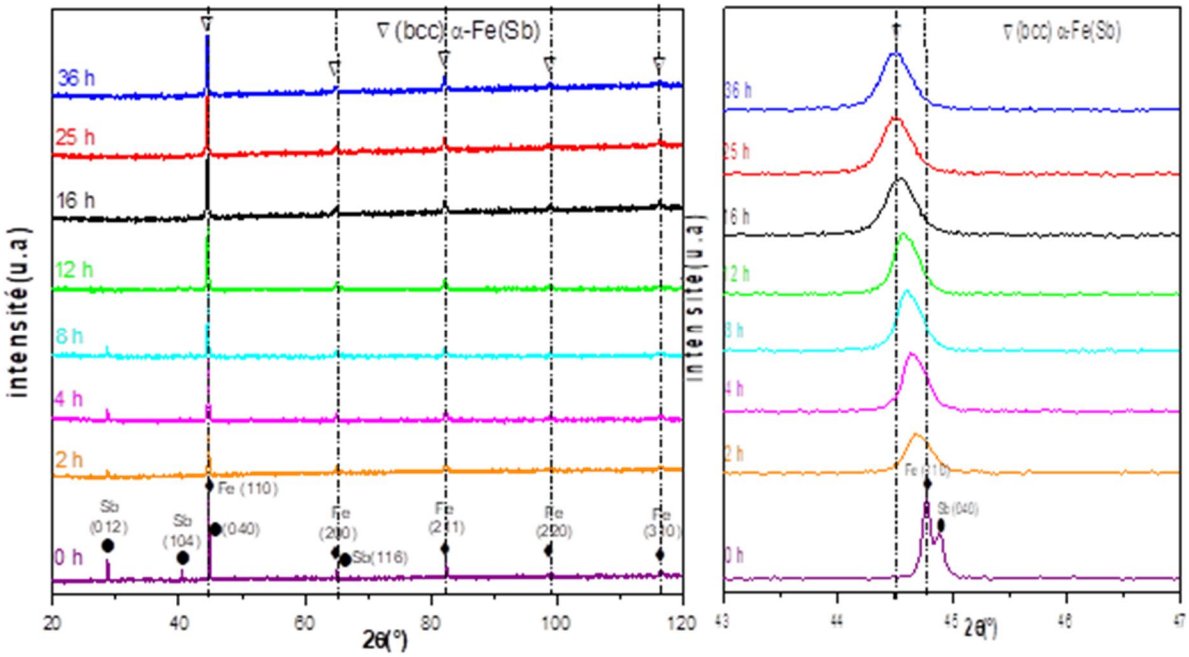

FIG. 1. (a) X-ray diffraction patterns of the $Fe_{90}Sb_{10}$ powders milled for different milling times. (b) Deconvolution of the most intense peak for different milling time.

In Fig. 2, the evolution of the average crystallite size <D> (nm) and the root mean square microstrain $< \sigma^2 >^{\frac{1}{2}}$ is presented as a function of milling duration, based on X-ray diffraction (XRD) analysis performed using the Rietveld refinement method with the MAUD software. The data indicate that as the milling time increases from 0 to 36 hours, the crystallite size <D> decreases significantly from 59.95 nm to 18.16 nm, while the microstrain $< \sigma^2 >^{\frac{1}{2}}$ increases from 0.076% to 0.19%. This inverse relationship suggests that prolonged milling induces increased lattice distortion and grain refinement. The observed grain size reduction is attributed to the enhanced hardness of the FeSb powders during mechanical alloying, which promotes more efficient fragmentation and refinement of crystallites [20].

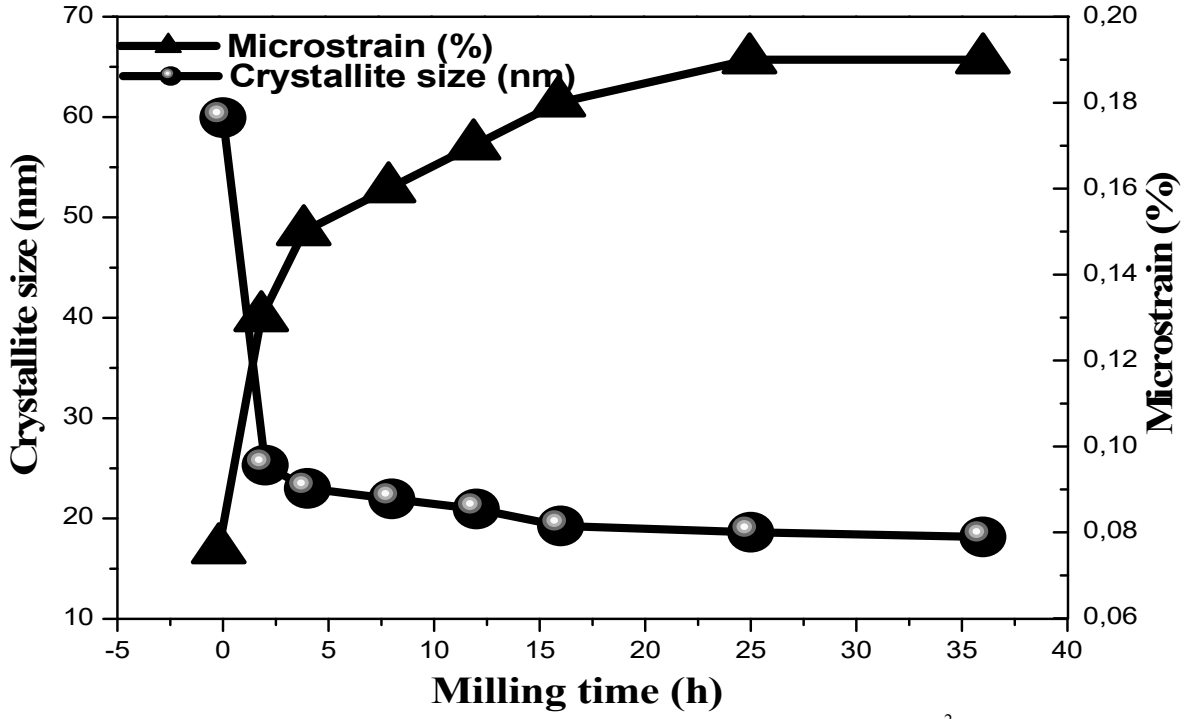

FIG. 2. Evolution of the average crystallite size, <*D*>(nm), and mean internal strain<σ^2>1/2 (%),of $Fe_{90}Sb_{10}$ powders versus milling time.

With the progression of milling times, there are noticeable alterations in the morphological structure of the macroscopic powders, as evidenced by the SEM micrographs in Fig. 3 where SEM images show the particles of $Fe_{90}Sb_{10}$ powders after undergoing mechanical alloying for durations of 25 hours and 36 hours.

For the 25-hour milling duration, as depicted in Fig. 3(a), a noticeable transformation occurs in which the ground particles become smaller. Fine particles, approximately 5 µm in size, emerge, exhibiting a relatively uniform appearance indicating a balance between fracture and welding phenomena. During this stage, the bonding forces between powder particles are enhanced as grain size decreases, primarily due to increased surface contact, defect-induced reactivity, and improved atomic diffusion at the interfaces. Deformations are no longer easily achievable as they demand a substantial force for fracturing the particles. The grain size decreases over the milling time, which is attributed to the interplay of fracture and welding processes resulting from the collisions between the powder, milling balls, and the inner wall of the container. At the 36-hour mark of milling (as shown in Fig. 3(b)), large agglomerates are observed comprising exceedingly fine particles. These particles demonstrate a further refinement, becoming even finer and smaller with increased milling duration [21]. These findings indicate that after 36 hours of milling, significantly smaller agglomerates are obtained compared to the preceding times, with the individual particles displaying greater homogeneity. It is noteworthy that, at this stage, the fracture process takes precedence in the mechanosynthesis, leading to a notable reduction in particle size.

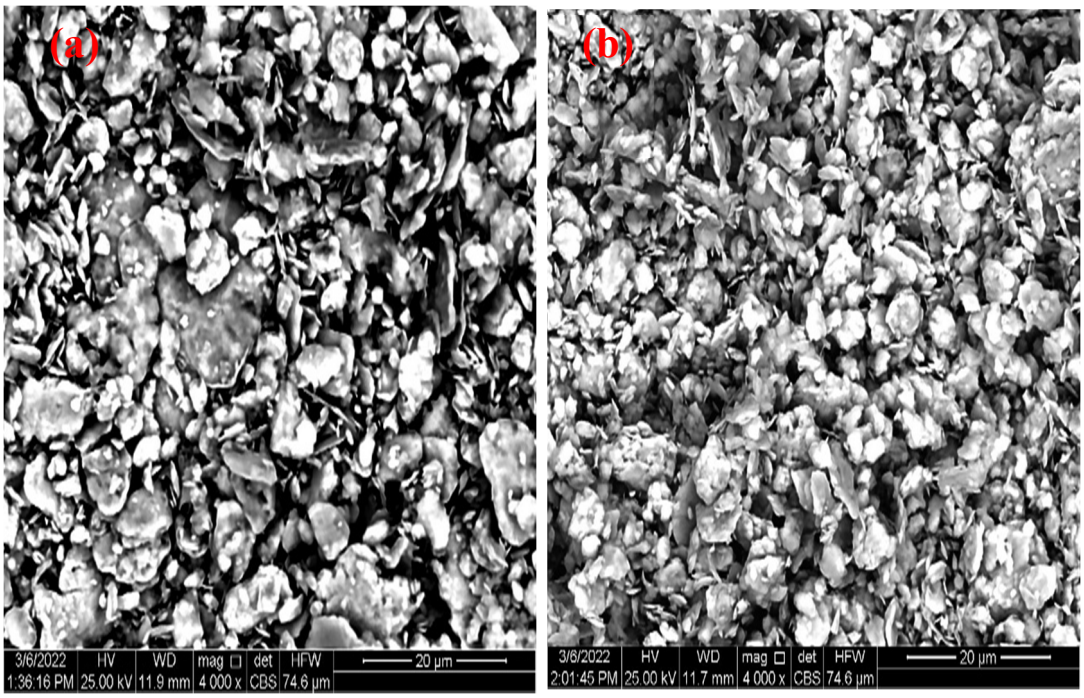

FIG. 3. SEM images showing the shape evolution of the $Fe_{90}Sb_{10}$ powder mixtures at different milling times (a) 25 h, and (b) 36 h, respectively.

The sigmoid-shaped hysteresis loops shown in Fig. 4 are typical of nanostructured magnetically soft materials, where the reduction in grain size leads to the formation of single-domain particles and low coercivity. The magnetic behavior is influenced by structural characteristics such as lattice strain, grain boundary density, and crystallite size, all of which affect the magnetization process and the motion of domain walls. These loops (see inset) reflect the reduced coercive field and low hysteresis losses, properties highly desirable in soft magnetic materials. Such behavior is further influenced by structural distortions within the grains, which facilitate domain wall motion. These combined effects contribute to improved energy efficiency, making these materials promising candidates for applications in power electronics, sensors, and magnetic storage technologies [19].

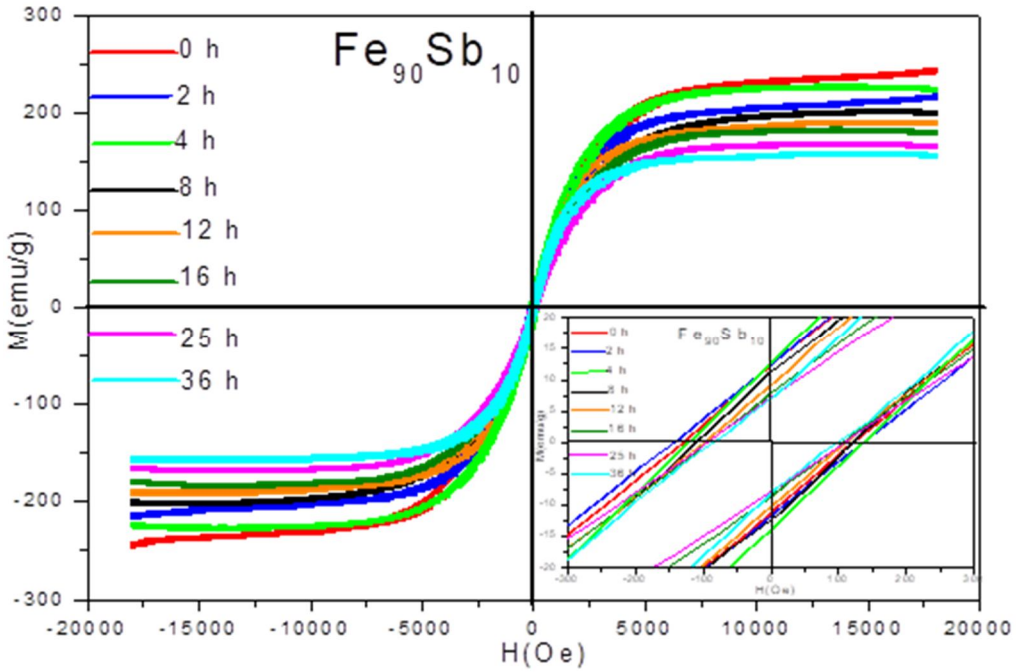

FIG. 4. Hysteresis loops (M–H curves) at room temperature of the $Fe_{90}Sb_{10}$ powders milled for a 0, 2, 4, 8, 12, 16, 25, and 36 h.

3.2. Fe–10Sb (wt.%) Thin Films

Figure 5 illustrates the X-ray diffraction patterns of the solid solution of $Fe_{90}Sb_{10}$ films obtained by evaporation onto glass substrates with varying thicknesses. The selected powder, subjected to 25 hours of grinding, was used in the process. For the sample with a thickness of 16 nm, a single peak emerged, displaying a relatively low intensity. This peak, positioned at an angle of 2θ = 44.65°, was assigned to the (110) reflection of the body-centered cubic (bcc) α-Fe(Sb) solid solution. Upon increasing the thickness to 25 nm, the emergence of the (110) peak is accompanied by the appearance of a slightly intensified peak corresponding to the (200) plane of the α-Fe(Sb) phase. For the thicker films with thicknesses of t = 60 nm and t = 90 nm, besides the presence of the (110) peak, additional peaks at 2θ = 65.10° and 82.31° appeared. These peaks have been identified as corresponding to the (200) and (211) planes of the α-Fe(Sb) phase, respectively. The distinct peaks observed in the X-ray diffraction patterns as the film thickness increases suggest notable variations in the crystallographic structure. These peaks, representing specific planes, serve as indicators of the crystalline orientation within the $Fe_{90}Sb_{10}$ films. The prominence of certain crystallographic planes, such as (110), underscores the evolving nature of the α-Fe(Sb) phase in response to changes in thickness. Understanding the structural characteristics of these films is of paramount importance. The arrangement of atoms in the crystal lattice, as revealed by the presence and intensity of these peaks, provides crucial insights. This information can guide further investigations into the properties and applications of $Fe_{90}Sb_{10}$ films across different thicknesses. The evolving nature of the α-Fe(Sb) phase suggests a dynamic relationship between film thickness and crystallographic behavior. This relationship may be influenced by factors such as strain, defects, or variations in the deposition process. By unravelling these connections, researchers can gain a deeper understanding of the material's behavior and tailor its properties for specific applications. The significance of this information extends to practical implications. Tailoring the film thickness could serve as a strategic approach for engineering desired properties in $Fe_{90}Sb_{10}$ films. Whether for applications in sensors, electronic devices, or other technological advancements, a comprehensive understanding of the structural characteristics is essential.

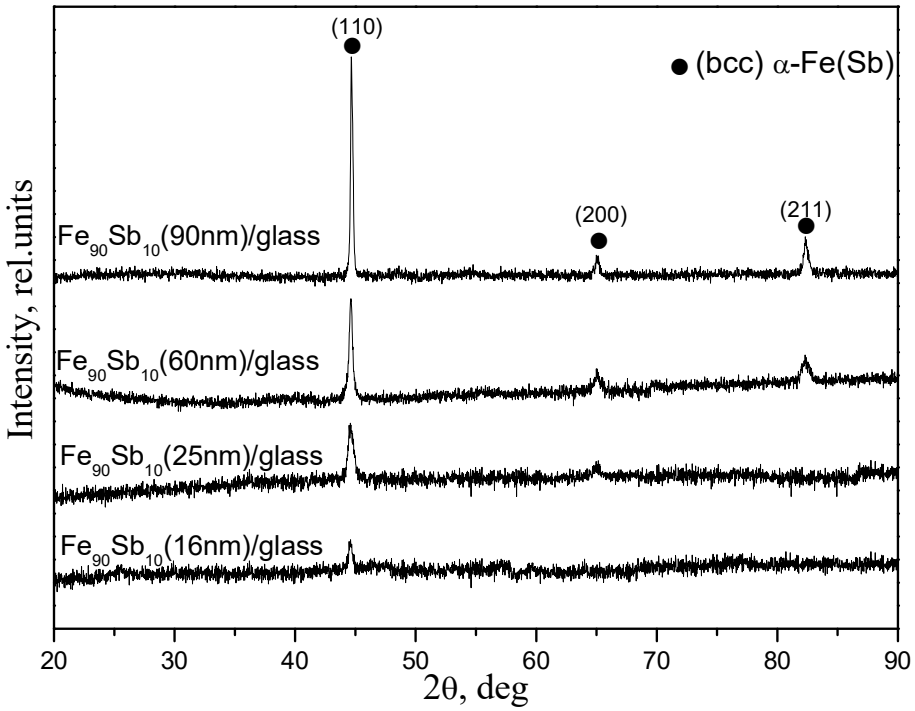

FIG. 5. X-ray diffraction spectra of $Fe_{90}Sb_{10}$ films for various thicknesses.

The lattice parameter is a crucial factor as it offers insights into the state of stresses imposed on the thin layer. The changes in lattice parameters across all samples, influenced by thickness, were identified through the Rietveld refinement of the X-ray diffraction spectrum, as illustrated in Fig. 6.

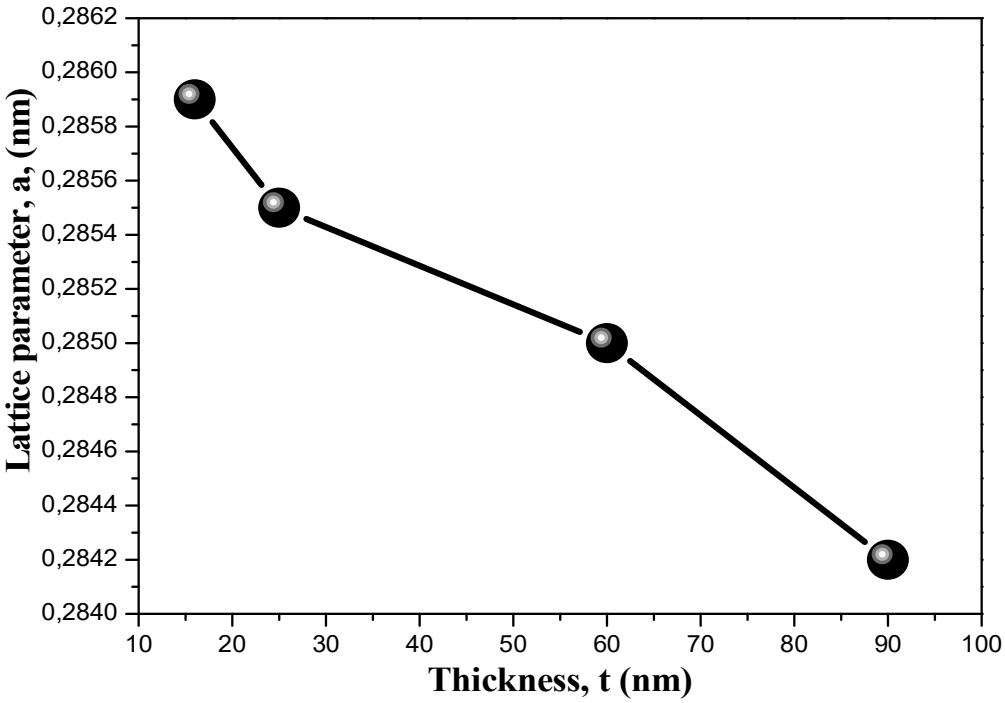

FIG. 6. Variations in the lattice parameter, denoted as a (nm), with changes in the thickness of $Fe_{90}Sb_{10}$ films.

Figure 6 illustrates how the lattice parameter a (nm) monotonically decreases with the increase of thickness. Specifically, the value of a (nm) ranges from (0.2859 ± 0.0001) nm for the 16 nm film to (0.2841 ± 0.0001) nm for the 90 nm film. Additionally, it is noteworthy that these values are below the bulk value, which equals 0.2866 nm [22]. Sabrina Lamrani et al. [23] have previously reported a similar trend in the behavior of "a" (Å) concerning film thickness. This study utilized thermal evaporation for a $Ni_{80}Fe_{20}$ alloy, considering thicknesses of 16, 25, 60, and 90 nm.

The observed monotonic decrease in the lattice parameter with increasing thickness suggests a systematic trend in the crystal structure. The reduction in "a" indicates a possible compression or contraction of the lattice as the film thickness grows. This phenomenon could be influenced by factors such as strain, defects, or variations in the growth conditions during film deposition. Furthermore, the observed values being below the bulk value suggests that the thin films may undergo structural modifications or distortions compared to their bulk counterpart. This deviation could arise from factors like surface effects, interface interactions, or other size-dependent phenomena.

The mean size of the crystallite <D> is expressed as:

$$< D >= K \frac{\lambda}{\beta_L cos\theta} \quad (1)$$

The integral width of the Lorentzian component, denoted as β_L, is utilized, with λ representing the wavelength of the radiation employed. In the course of Rietveld refinement, the parameter subject to adjustment is <D>.

The difference between the value of the lattice parameter measured by X-ray diffraction and the value of the $Fe_{90}Sb_{10}$ bulk material gives the microstrain ε (%):

$$\varepsilon = \frac{a_{mesured} - a_{bulk}}{a_{bulk}} \quad (2)$$

Figure 7 shows the evolution of the average crystallite size <D> and microstrain ε of $Fe_{90}Sb_{10}$ films evaporated on glass substrates with thicknesses of 16 nm, 25 nm, 60 nm, and 90 nm. From the figure, <D> increases from 5.9 nm for the thinnest film to 16.8 nm for the thickest one, indicating a clear trend of grain growth. This behavior is typical of evaporated metallic and alloy thin films, where increased thickness corresponds to longer deposition times and enhanced adatom mobility, favoring processes such as island coalescence, surface diffusion, and grain-boundary migration. These mechanisms reduce the total grain-boundary area and promote the formation of larger, more ordered crystalline domains.

The microstrain values obtained from Eq. (2) are systematically negative, changing from −0.0024 % to −0.0083 % as thickness increases. The negative sign indicates compressive strain

within the lattice, and the observed increase in its absolute magnitude suggests that thicker films retain progressively higher residual compressive stresses. This trend is somewhat counterintuitive, as thicker films are often expected to partially relax interfacial stresses and approach the structural state of bulk material. In the present case, the increase in compressive strain may be linked to the accumulation of intrinsic growth stress during deposition, driven by persistent lattice mismatch with the glass substrate, thermal-expansion coefficient differences, defect incorporation, and grain-boundary densification that hinders stress relaxation.

The simultaneous increase of <D> and compressive |ε| reflects a complex interplay between microstructural coarsening and stress development. While grain growth reduces grain-boundary density, intrinsic compressive stress can continue to build up through defect generation and microstructural densification during prolonged deposition. This combined evolution of crystallite size and residual stress is expected to influence the functional properties of $Fe_{90}Sb_{10}$ films, particularly through magnetoelastic coupling, adhesion strength, and potential stability under mechanical or thermal cycling. Thickness control therefore emerges as a critical parameter for tailoring both structural and functional performance in such nanostructured alloys.

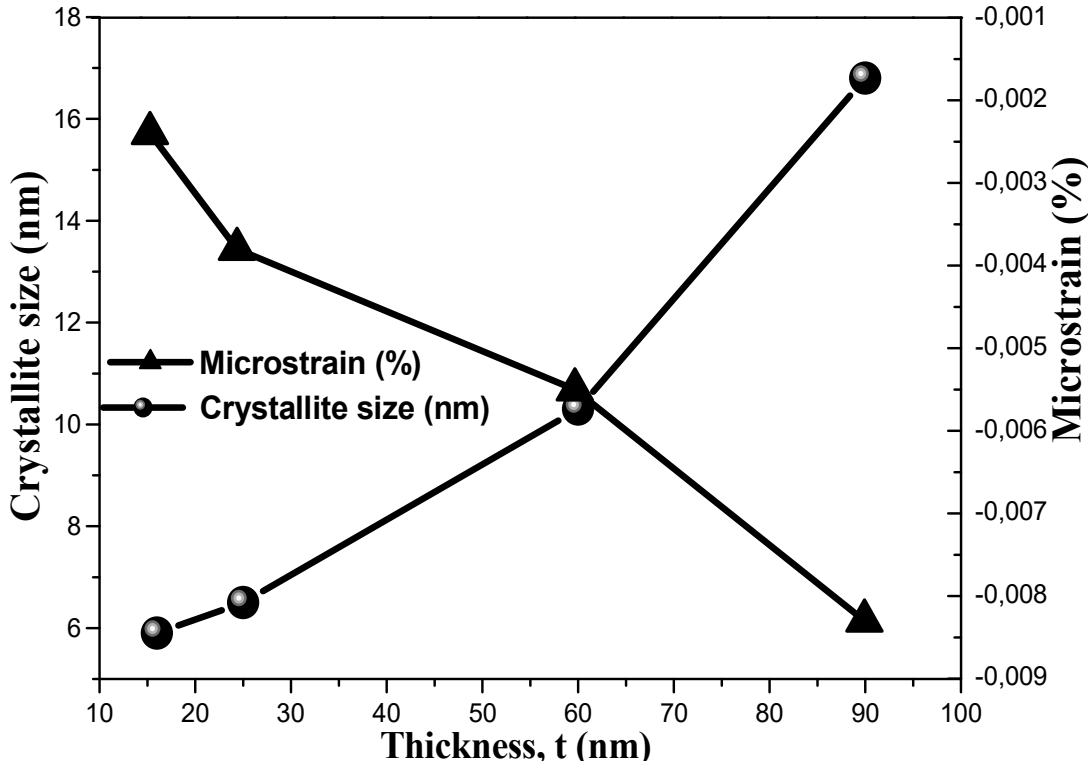

FIG. 7. Evolution of the average crystallite size, <*D*>(nm), and microstrain ε (%) of $Fe_{90}Sb_{10}$ films vs. thickness.

Figure 8 displays SEM surface images depicting variations in thickness for $Fe_{90}Sb_{10}$/glass. For the image in Fig. 8(a) corresponding to a $Fe_{90}Sb_{10}$/glass film with a thickness of 16 nm, a clear depiction of a consistently even surface is observed. Limited features can be observed due to the small grain size of this sample, which is D = 5.9 nm. While for the films with thicknesses 25 and 60 nm, small rounded shape droplets appear on the surface, as illustrated in Figs. 8(b) and (c). This suggests a change in the surface morphology as the film thickness increases. In the case of the thickest film, with a thickness of 90 nm, Fig. 8(d) displays a notable increase in the number of smaller rounded droplets scattered across the surface. This observation indicates a substantial alteration in the surface characteristics as the film thickness increases.

The process of fabricating $Fe_{90}Sb_{10}$/glass films involves a crucial phase where Fe(Sb) solid solution powder undergoes a transformation. During the evaporation of iron powder, a transition from the solid to the liquid state occurs, generating a liquid phase of the material. This pivotal moment is followed by a phenomenon known as the "jet of droplets". In this step, droplets of the liquid material, resulting

from the evaporation of Fe(Sb) solid solution powder, are propelled towards the substrate with kinetic energy. The substrate, which may consist of glass in our study, plays an important role in the process. Upon contacting the substrate, the droplets undergo a nearly instantaneous process of cooling and solidification. This rapid cooling leads to the formation of small circular grains, also known as "droplets," on the substrate's surface. These grains exhibit distinct morphology, influenced by the speed of the droplet jet, temperature, and other processing parameters. Thus, the phenomenon of circular grains is the result of a complex sequence of evaporation, transformation into the liquid phase, droplet projection, and finally, rapid cooling upon contact with the substrate. These observations, illustrated in the SEM images in Fig. 8, provide valuable insights into the dynamic processes during the fabrication of $Fe_{90}Sb_{10}$/glass films at different thicknesses.

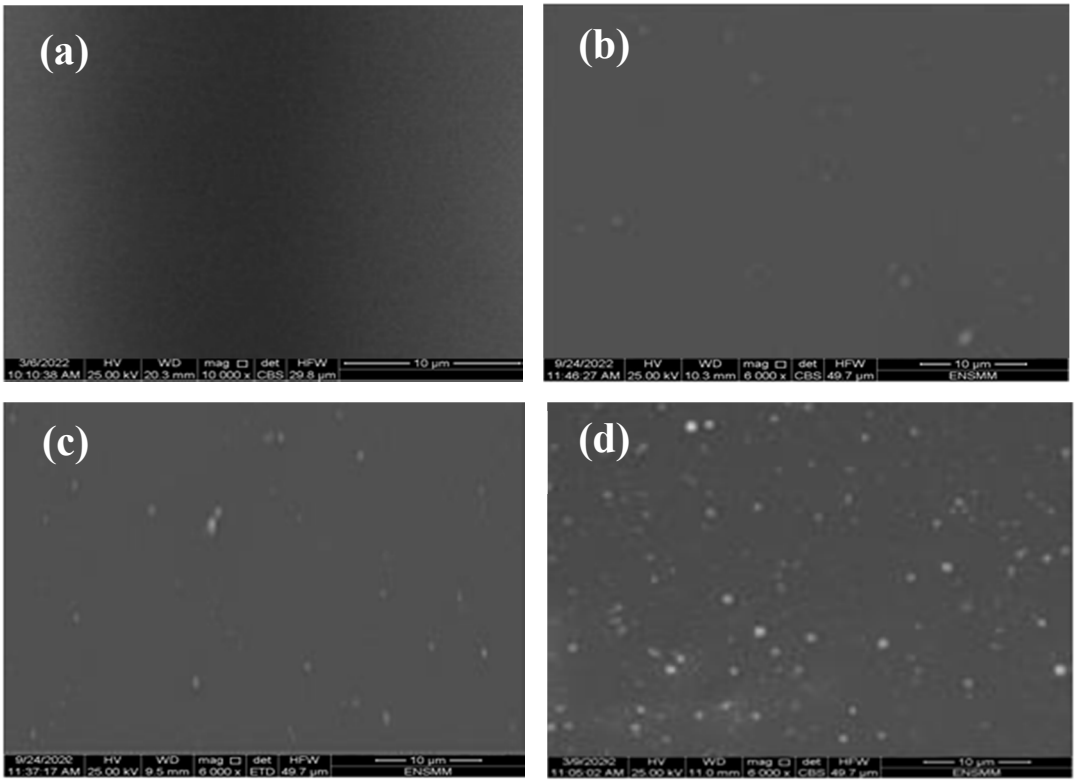

FIG. 8. SEM images of $Fe_{90}Sb_{10}$ /glass for thicknesses of: (a) 16 nm, (b) 25 nm, (c) 60 nm, and (d) 90 nm.

Figure 9 displays the hysteresis loops for (bcc) α-Fe (Sb) films on glass with varying thicknesses, measured at room temperature. These curves were acquired in the parallel configuration, with the magnetic field (H) aligned in the film plane. It is found that all hysteresis loops are saturated and have a sigmoidal shape. The low hysteresis loss observed in the cycling between -H and +H is indicative of low energy loss within the system. This phenomenon is closely linked to the soft magnetic characteristics exhibited by the layer. Soft magnetic materials are known for their ability to undergo rapid and reversible magnetization changes with minimal energy dissipation. In the context of the discussed layer, this property contributes to the overall efficiency of the material in terms of energy consumption during the cycling process. The soft magnetic nature allows the material to easily realign its magnetic domains in response to changing external magnetic fields, thereby minimizing the energy losses associated with hysteresis. This property is particularly advantageous in applications where energy efficiency and precise control of magnetic behavior are critical factors.

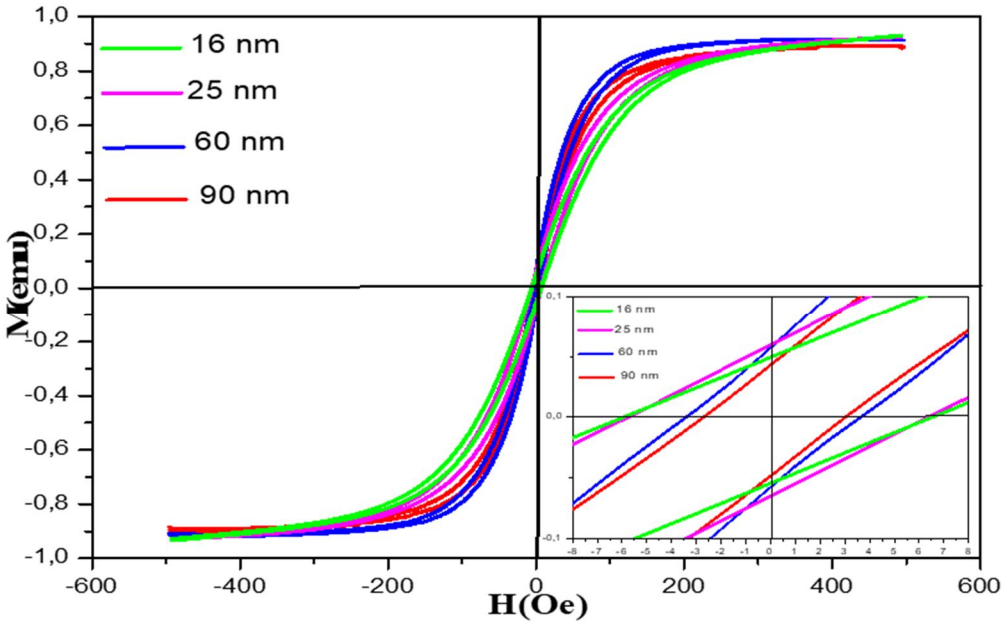

FIG. 9. Hysteresis loops for α-Fe (Sb) on glass with various thicknesses: 16 nm, 25 nm, 60 nm, and 90 nm.

Figure 10 illustrates the variation of the coercive field (H_c) as a function of film thickness, with measured values ranging from 3.05 to 6.64 Oe. A systematic decrease in H_c is observed as the thickness increases from 16 nm to 90 nm, indicating a strong thickness dependence of the magnetic response.

The coercive field is a fundamental parameter describing the resistance of a magnetic material to magnetization reversal, as obtained from the width of the magnetic hysteresis loop. It is determined by the balance between domain wall motion, domain nucleation, and magnetic anisotropy contributions, which are all influenced by the microstructural characteristics of the film.

The observed decline in H_c with increasing thickness can be attributed to several interconnected factors. In ultrathin films, surface and interface effects play a dominant role in determining the magnetic properties. At lower thicknesses (e.g., 16 nm), a higher fraction of atoms is located near the film interfaces, where broken symmetry, strain, and surface roughness introduce strong pinning sites for domain walls. These localized pinning centers increase the energy barrier for domain wall movement, resulting in a higher coercive field. Furthermore, surface-induced magnetic anisotropy tends to be more pronounced in thin layers, contributing to the observed magnetic hardening.

As the film thickness increases, the relative contribution of these surface and interface effects diminishes, while the bulk-like behavior of the film becomes more prominent. In thicker layers (above ~60 nm), domain wall motion is facilitated by a more continuous and less defect-dominated magnetic environment. The larger film volume accommodates more extensive magnetic domains and longer domain walls, which can realign more easily under an applied magnetic field. This reduction in effective pinning density leads to a more efficient magnetization reversal process and consequently a lower coercive field.

In addition to domain structure evolution, strain relaxation also plays an important role. Mechanical stresses induced during thin film growth can significantly affect magnetic anisotropy through magnetoelastic coupling. Thicker films tend to exhibit partial relaxation of growth-induced strain, which reduces magnetoelastic contributions to coercivity. This structural relaxation, combined with a reduction in surface anisotropy, further enhances magnetic softening with increasing thickness.

The present results are consistent with previous findings in metallic and oxide thin films, where Hc decreases with thickness due to the combined effects of reduced surface/interface anisotropy, improved domain wall mobility, and diminished pinning from structural defects [24-26]. This behavior underscores the critical role of thickness control in tailoring the magnetic properties of thin films for applications in sensors, spintronic devices, and magnetic recording media [27].

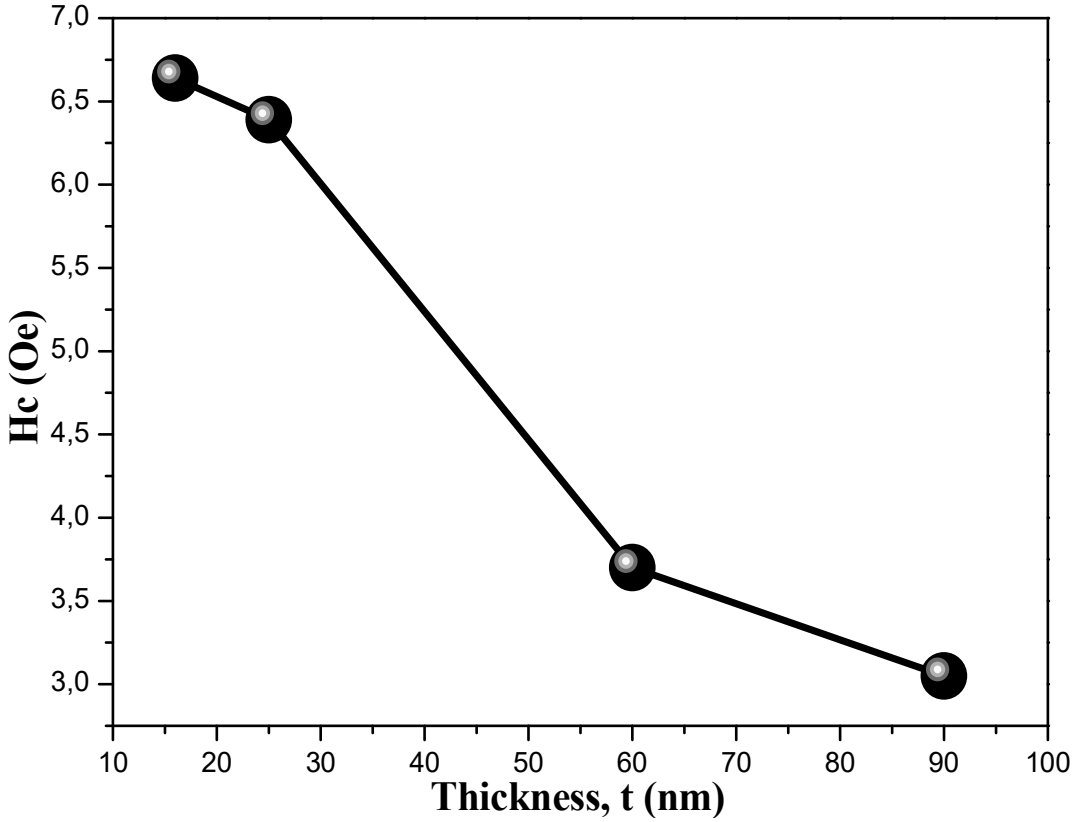

FIG. 10. Hysteresis loops for α-Fe (Sb) on glass with various thicknesses: 16 nm, 25 nm, 60 nm, and 90 nm.

4. Conclusions

Thin films of the $Fe_{90}Sb_{10}$ solid solution were synthesized by thermally evaporating mechanically alloyed powder (25 hours of milling) onto glass substrates under high vacuum. X-ray diffraction analysis revealed that all films exhibit compressive residual stress, as evidenced by a reduction in lattice parameter compared to the bulk value (0.2866 nm). Such stress likely results from lattice deformation during the deposition process and the mismatch between film and substrate.

The crystallite sizes, refined using the Rietveld method, were found to range from 5.9 to 16.8 nm, indicating a nanocrystalline structure. These values are consistent with a high degree of structural coherence but do not support the use of the term "monocrystalline."

From a magnetic perspective, the coercive field (Hc) decreases with increasing thickness, from 6.64 Oe at 16 nm to 3.05 Oe at 90 nm. This trend reflects the reduced influence of surface and interface anisotropies in thicker films, along with improved crystallinity and enhanced domain wall mobility, leading to lower coercivity and a more bulk-like magnetic behavior.

These results collectively highlight the strong interdependence between the structural and magnetic properties of Fe-Sb thin films and their sensitivity to synthesis parameters such as film thickness and precursor microstructure.

Acknowledgments

The authors thank the members of group L3M-Annaba, Dr. S. Leboub, M. Mittri, and H. Zedouri, for acquiring SEM pictures. This work was supported by Algerian Directorate for Scientific Research and Technological Development (DGRSDT).

References

[1] Kang, I., Yang, J., Lee, W., Seo, E.Y., and Lee, D.H., Technology in Society, 74 (2023) 102326.

[2] Schummer, J., Scientometrics, 59 (3) (2004) 425.

[3] Islam, N. and Miyazaki, K., Technological Forecasting and Social Change, 76 (1) (2009) 128.

[4] Wang, A.P., Hou, C.E., and Hung, S.W., Nanotechnology, 7 (3) (2018) 233.

[5] Zhanga, Y.H., Wuc, L.R., Maa, J., and Cui, G., Next Nanotechnology, 2 (2023) 100011.

[6] Pan, F., Song, C., Liu, X.J., Yang, Y.C., and Zeng, F., Materials Science and Engineering R: Reports, 62 (2008) 1.

[7] Ramasubramanian, S., Thangavel, R., Rajagopalan, M., Thamizhavel, A., Asokan, K., Kanjilal, D., and Kumar, J., Current Applied Physics, 13 (2013) 1547.

[8] Hoffmann, W. and Pellkofer, T., Thin Solid Films, 520 (12) (2012) 4094.

[9] Chatzisideris, M.D., Espinosa, N., Laurent, A., and Krebs, F., Solar Energy Materials and Solar Cells, 156 (2016) 1.

[10] Yoonho, A. and Jong, Y.S., Journal of Materials Research and Technology, 18 (2022) 2232.

[11] Ghebouli, B., Layadi, A., and Kerkache, L., European Physical Journal Applied Physics, 3 (1998) 35.

[12] Szmaja, W., Balcerski, J., Kozłowski, W., Cichomski, M., Grobelny, J., Smolny, M., and Kowalczyk, P.J., Journal of Alloys and Compounds, 521 (2012) 174.

[13] Wang, S., Gao, T., Wang, C., and He, J., Journal of Alloys and Compounds, 554 (2013) 405.

[14] Choi, J.G., Hwang, D.G., Rhee, J.R., and Lee, S.S., Journal of Magnetism and Magnetic Materials, 322 (2010) 2191.

[15] Hea, Y., Fanc, C., and Lee, S.T., Nano Today, 5 (2010) 213.

[16] Lutterotti, L., "Laboratorio Scienza e Tecnologia dei Materiali". (Universita di Torino, Corso, 2000).

[17] Branger, V., Briand, E., Kusmeruck, C., Morin, N., Corot, F., and Auburtin, Ph., Journal de Physique IV, France, 12 (2002) 165.

[18] Boukherroub, N., Guittoum, A., Souami, N., Akkouche, K., and Boutarfaia, S., EPJ Web of Conferences, 29 (2012) 00010.

[19] Guemmoud, N., Hafs, A., and Hafs, T., International Journal of Advanced Manufacturing Technology, 122 (2022) 2043.

[20] Davis, R.M., Dermont, B.M., and Koch, C.C., Metallurgical and Materials Transactions A, 19 (1988) 2867.

[21] Hasnaouia, N., Hafs, A., Hafs, T., and Bendjedaa, F., Journal of Alloys and Compounds, 899 (2022) 163338.

[22] Yeh, T., Sivertsen, J.M., and Judy, J.H., IEEE Transactions on Magnetics, 23 (1987) 2215.

[23] Lamrani, S., Guittoum, A., Schafer, R., Pofahl, S., Neu, V., Hemmous, M., and Benbrahim, N., European Physical Journal Applied Physics, 74 (2016) 30302.

[24] Sun, S., Murray, C.B., Weller, D., Weller, Folks, L., and Moser, A., Science, 287 (2000) 1989.

[25] Bernhard, T., Baron, M., Gruyters, M., and Winter, H., Surface Science, 600 (2006) 1877.

[26] Javed, A., Morley, N.A., and Gibbs, M.R.J., Applied Surface Science, 257 (13) (2011) 5586.

[27] Bensehil, I., Kharmouche, A., and Bourzami, A., Journal of Superconductivity and Novel Magnetism, 30 (2017) 795.